NOVA SCHOOL OF SCIENCE & TECHNOLOGY

DEPARTAMENT OF MATERIALS SCIENCE

RODRIGO ALEXANDRE GOMES PEDRO

BSc in Materials Engineering

DISSIMILAR WELDING OF AS-CAST AlCoCrFeNi$_{2.1}$ EUTECTIC HIGH ENTROPY ALLOY WITH 316 STAINLESS STEEL AND INCONEL 718

MASTER IN MATERIALS ENGINEERING

NOVA University Lisbon

October, 2024

DEPARTAMENT OF
MATERIALS SCIENCE

DISSIMILAR WELDING OF AS-CAST AlCoCrFeNi$_{2.1}$ EUTECTIC HIGH ENTROPY ALLOY WITH 316 STAINLESS STEEL AND INCONEL 718

RODRIGO ALEXANDRE GOMES PEDRO

BSc in Materials Engineering

Adviser: Professor Doutor João Pedro de Sousa Oliveira
Full Professor, School of Science & Technology, NOVA University Lisbon

Co-advisers: Jiajia Shen
Postdoctoral Researcher, School of Science & Technology, NOVA University Lisbon

Examination Committee:

Chair: Doutor Rui Jorge Cordeiro Silva,
Associate Professor, School of Science & Technology, NOVA University Lisbon

Adviser: Doutor João Pedro de Sousa Oliveira,
Full Professor, School of Science & Technology, NOVA University Lisbon

Members: Doutor Ivan Rodolfo Pereira Garcia de Galvão,
Assistant Professor, Instituto Superior de Engenharia de Lisboa

MASTER IN MATERIALS ENGINEERING

NOVA University Lisbon
October, 2024

Dissimilar welding of as-cast AlCoCrFeNi$_{2.1}$ Eutectic high entropy alloy with 316 stainless steel and Inconel 718

Aos meus pais e ao meu avô Franco.

ACKNOWLEDGMENTS

First of all, I would like to leave my sincerest appreciations to my supervisor, Professor João Oliveira, for the chance to embrace this challenge, for all the advices and clear directions provided every step of the way, and above all for the availability demonstrated and given throughout this year.

Second, to my co-supervisor, Doctor Jiajia Shen, for her support, knowledge, fruitful discussions and invaluable assistance during the whole experimental part of the thesis project.

I also must acknowledge Jaivindra, Liu, Nithin, and Hugues for their relevant help, expertise in welding processes, and for teaching me crucial theory and practical knowledge.

I would also like to express my gratitude to my laboratory colleague Inês, for the immeasurable support in every matter concerning this thesis, meaningful discussions, and shared challenges during these last few months.

My heartfelt gratitude to my dear friends, Diogo, Marcelo and Pedro for all the support and encouragement during the hard times and for the happy and laughter moments during these long-lasting friendships. A special thanks to my friend and roommate Vlad, for the companionship and joyful memories since the first year of university. Without them this journey would have not been the same.

Lastly and most importantly, I would like to thank my family, especially my parents for the financial, boundless support, kindness and sacrifices in providing the best resources and education that I have always desired. I hope I can give back to them in the future.

“If everything seems under control, you’re not going fast enough.” (Mario Andretti).

ABSTRACT

During the last few years, high entropy alloys (HEA) have received increasing attention owing to their remarkable characteristics and mechanical properties, emerging as novel engineering alloys for multiple functional and structural applications. Recently, gas tungsten arc welding (GTAW) was successfully attempted for the first time on an $AlCoCrFeNi_{2.1}$ eutectic high entropy alloy (EHEA). However, dissimilar welding of EHEAs is still scarce. During the non-equilibrium fusion dissimilar welding, mixing of the liquid phases of two materials with distinct thermophysical properties can promote the generation of undesirable and detrimental phases. To bridge this gap, and pave the way for potential structural applications, GTAW technique was employed to weld the $AlCoCrFeNi_{2.1}$ EHEA with 316 stainless steel and Inconel 718, aiming to obtain defect-free welded joints. The effects of the GTAW technique on the microstructure and mechanical behavior were investigated and correlated by coupling optical microscopy, microhardness mapping, tensile tests and fracture surface analysis. Both joints displayed a heterogeneous microstructure in the fusion zone (FZ), varying from equiaxial to coarse elongated dendritic structures. The coarse grain morphology translated into lower hardness results across the FZ of the $AlCoCrFeNi_{2.1}$ EHEA/316 stainless steel joint. Conversely, in the $AlCoCrFeNi_{2.1}$ EHEA/Inconel 718 joint, a remarkable finding was the substantial increase in hardness along the molten pool, allowing to unveil a possible solid solution strengthening mechanism induced by the precipitates upon fusion of the Inconel 718. This mechanism justifies the increment in the ultimate tensile strength, compared to the $AlCoCrFeNi_{2.1}$ EHEA/316 stainless steel joint, while preserving most of the fracture strain (653 vs 432 MPa and 9.2 vs 9.7 %, respectively). Overall, both dissimilar joints showcased a promising strength and ductility synergy, establishing the potential of GTAW for the dissimilar welding of EHEAs to traditional metals, targeting structural applications.

Keywords: $AlCoCrFeNi_{2.1}$, Stainless Steels, Inconel 718, High Entropy Alloys, Gas Tungsten Arc Welding, Microstructure, Mechanical Properties.

RESUMO

Nos últimos anos, as ligas de alta entropia (HEA) têm suscitado um interesse crescente, dadas as suas características e propriedades mecânicas eminentes, surgindo como ligas de engenharia pioneiras para a implementação em diversas aplicações funcionais e estruturais. Recentemente, a soldadura com elétrodo não consumível de tungsténio sob proteção gasosa inerte (GTAW) foi com realizada com sucesso, pela primeira vez, numa liga eutéctica de alta entropia (EHEA) $AlCoCrFeNi_{2.1}$. No entanto, a soldadura dissimilar de EHEAs não têm constituído um alvo de investigação intensiva. Durante os processos de soldadura dissimilar por fusão, em condições de não equilíbrio, poderá verificar-se a ocorrência de fases indesejáveis e prejudiciais para a integridade estrutural da junta. De modo a colmatar esta lacuna, e promover a sua implementação em aplicações estruturais, o processo GTAW foi utilizado para soldar a EHEA $AlCoCrFeNi_{2.1}$ ao aço inoxidável 316 e ao Inconel 718, com o intuito de obter cordões de soldadura isentos de defeitos. Os efeitos da técnica GTAW na microestrutura e propriedades mecânicas da junta foram avaliados e correlacionados recorrendo a técnicas de microscopia ótica, avaliação de microdurezas, ensaios de tração, e análise das superfícies de fratura. Ambas as amostras evidenciaram uma microestrutura heterogénea na zona de fusão (FZ), caracterizada por estruturas dendríticas equiaxiais e alongadas grosseiras. A morfologia de grãos grosseiros contribuiu para o decréscimo dos valores de dureza ao longo da ZF da junta $AlCoCrFeNi_{2.1}$ EHEA/aço inoxidável 316. Em oposição, na junta $AlCoCrFeNi_{2.1}$ EHEA/Inconel 718, constatou-se o aumento considerável das durezas ao longo da FZ, sugerindo a ocorrência do mecanismo de endurecimento por solução sólida, incitada pelos precipitados provenientes da fusão do Inconel 718. Este mecanismo justifica o incremento da tensão de rutura, comparativamente à junta $AlCoCrFeNi_{2.1}$ EHEA /aço inoxidável 316, preservando simultaneamente a extensão à fratura (653 vs 432 MPa e 9.2 vs 9.7 %, respetivamente). De um modo geral, ambas as juntas dissimilares exibiram um balanço promissor entre tensão de rutura e ductilidade, salientando o potencial do processo GTAW para a soldadura dissimilar de EHEAs a metais tradicionais, visando aplicações estruturais.

Palavras chave: $AlCoCrFeNi_{2.1}$, Aços Inoxidáveis, Inconel 718, Ligas de Alta Entropia, Soldadura por Arco Elétrico com Elétrodo de Tungsténio, Microestrutura, Propriedades Mecânicas.

CONTENTS

1 INTRODUCTION 1

1.1 High Entropy Alloys 1

1.1.1 High Entropy Alloys Core Effects 1

1.1.2 Eutectic High Entropy Alloys 2

1.2 Fusion Welding of High Entropy Alloys 3

1.2.1 Gas Tungsten Arc Welding 3

1.2.2 High Entropy Alloys Weldability 4

1.2.3 Dissimilar Welding of High Entropy Alloys 4

1.2.4 Eutectic High Entropy Alloys Weldability 5

1.3 State of the Art 5

2 MATERIALS AND METHODS 7

2.1 Materials 7

2.2 Methods 8

2.2.1 Gas Tungsten Arc Welding 8

2.2.2 Microstructural Analysis 8

2.2.3 Mechanical Analysis 9

3 RESULTS AND DISCUSSION 11

3.1 Optical Microscopy 11

3.2 Microhardness Measurements 15

3.3 Uniaxial Tensile Tests 18

3.4 Fracture Surfaces Analysis 20

4 CONCLUSIONS AND FUTURE WORK 23

LIST OF FIGURES

Figure 1.1 - Schematic illustration of Lattice Distortion Effect: (a) traditional alloy; (b) HEAs, adapted from [7] 2
Figure 1.2 - Schematic illustration of GTAW process [26]. 4
Figure 2.1 - Final Dissimilar welded joints: a) $AlCoCrFeNi_{2.1}$ EHEA / 316 stainless steel, b) $AlCoCrFeNi_{2.1}$ EHEA / Inconel 718 8
Figure 3.1 - Overview of the optical microscopy performed on the $AlCoCrFeNi_{2.1}$ EHEA/316 stainless steel dissimilar welded joint cross-section. 11
Figure 3.2 - Close up views of the regions marked in Figure 3.1: a) $AlCoCrFeNi_{2.1}$ EHEA BM; b) $AlCoCrFeNi_{2.1}$ EHEA HAZ; c) $AlCoCrFeNi_{2.1}$ EHEA FZ boundary; d) FZ; e) 316 stainless steel HAZ; f) 316 stainless steel BM. 12
Figure 3.3 - Overview of the optical microscopy performed on the $AlCoCrFeNi_{2.1}$ EHEA/ Inconel 718 welded joint cross-section. 13
Figure 3.4 - Close up views of the regions marked in Figure 3.3: a) $AlCoCrFeNi_{2.1}$ EHEA BM; b) $AlCoCrFeNi_{2.1}$ EHEA HAZ; c) FZ; d) Inconel 718 HAZ; e) Inconel 718 BM..... 14
Figure 3.5 - a) Microhardness color map across the $AlCoCrFeNi_{2.1}$ EHEA/316 stainless steel dissimilar welded joint; b) Microhard-ness profile obtained at mid height of the welded joint. 15
Figure 3.6 – a) Microhardness color map across the $AlCoCrFeNi_{2.1}$ EHEA/Inconel 718 dissimilar welded joint; b) Microhardness pro-file obtained at mid height of the welded joint. 17
Figure 3.7 - Representative uniaxial test stress-strain curves for the $AlCoCrFeNi_{2.1}$ EHEA/316 stainless steel and $AlCoCrFeNi_{2.1}$ EHEA/Inconel 718 dissimilar welded joints. 19
Figure 3.8 - SEM fractographs of the fracture surface of the AlCoCrFeNi2.1 EHEA/316 stainless steel specimens after the tensile test: a) Overview; b) Close up views of the region marked in a). 20
Figure 3.9 - SEM fractographs of the fracture surface of the $AlCoCrFeNi_{2.1}$ EHEA/ Inconel 718 specimens after the tensile test: a) Overview; b) Close up views of the region marked in a). 21

LIST OF TABLES

Table 1 - Chemical composition (in aspect ratio of at. %) of the base materials used in the samples. ... 7
Table 2 - Process parameters for the dissimilar welding of the $AlCoCrFeNi_{2.1}$ EHEA with 316 stainless steel / Inconel 718 ... 8
Table 3 - Summary of the base materials mechanical properties. ... 18
Table 4 - Summary of the welded joints mechanical properties. ... 20

ACRONYMS

BCC	Body-Centered Cubic
BM	Base Material
CNC	Computer Numerical Control
DIC	Digital Image Correlation
EBSD	Electron Backscatter Diffraction
EBW	Electron Beam Welding
EDS	Energy Dispersive X-Ray Spectroscopy
EHEA	Eutectic High Entropy Alloy
FCC	Face-Centered Cubic
FSW	Friction Stir Welding
FZ	Fusion Zone
GTAW	Gas Tungsten Arc Welding
HAZ	Heat Affected Zone
HEA	High Entropy Alloy
LBW	Laser Beam Welding
SEM	Scanning Electron Microscopy
XRD	High Energy Synchrotron X-Ray Diffraction

SYMBOLS

$\boldsymbol{\sigma_u}$	Ultimate tensile strength
$\boldsymbol{\varepsilon_f}$	Fracture strain
$\boldsymbol{\delta}$	Orthorhombic phase

1

INTRODUCTION

1.1 High Entropy Alloys

The development of alloys using a single base element dates back to the Bronze age. This method starts with a single main element, followed by the integration of reduced proportions of alloying elements to further improve the material microstructure and properties. By broking the prevailing paradigm of conventional alloys, of using only one or two principal elements, the concept of high entropy alloys (HEAs) was first presented in 2004 by Yeh et al. [1] and Cantor et al. [2]. This novel alloy design concept is typically composed of at least five main elements, with an atomic fraction of each element range between 5% to 35%, associated to a high mixing entropy in their liquid phase or high temperature solid solution phase [3,4].

1.1.1 High Entropy Alloys Core Effects

In 2006, as purposed by Yeh [4], the composition of the primary multicomponents and subsequent formation of single-phase solid states are governed by four core effects:

The High Entropy Effect, involves the increment in configurational mixing entropy, triggered by the increase in the number of constituent elements, which in turn would reduce the free energy of the alloy system. Such effect allows to stabilize the formation of simple solid solution phases (being the face-centered cubic (FCC) and the body-centered cubic (BCC) the prevalent structures), preventing the formation of brittle intermetallic compounds [5,6].

The Lattice Distortion Effect is associated to the discrepancy of the element sizes, randomly distributed in the lattice site, as shown in Fig 1.1. The absence of a dominant element promotes the distortion of the crystal structure, increasing the system internal free energy and affecting the properties of the alloy [4].

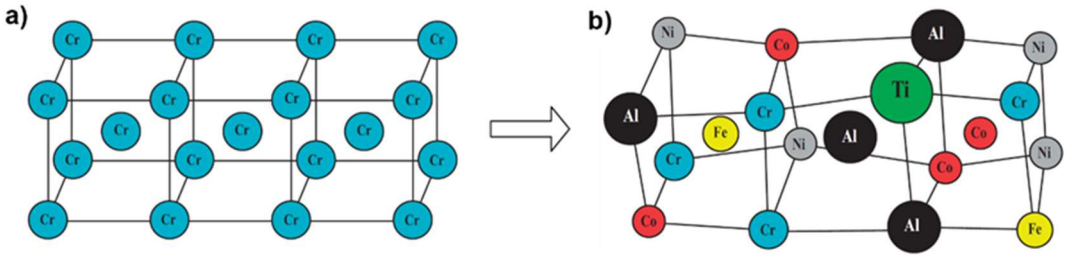

Figure 1.1 - Schematic illustration of Lattice Distortion Effect: (a) traditional alloy; (b) HEAs, adapted from [7]

The Sluggish Diffusion Effect has a dominant effect on the morphology and microstructure of HEAs by preventing the elements atomic diffusion, thus restricting the phase transformation [8]. This phenomenon has been recorded to increment the recrystallization temperature, promoting the formation of nanocrystalline and amorphous structures [9].

Finally, the Cocktail Effect, first introduced by Ranganathan [10], suggests that the selection of different elements can originate synergistic and unexpected properties, which could not be obtained from any one independent element. In this case, HEAs properties can be greatly modulated and enhanced by changing their chemical composition [11].

Considering the features derived from the above-mentioned effects, HEAs have paved the way to generate outstanding properties, owing to a wide range of possible compositions and combinations, making them particularly interesting in promising applications. HEAs exhibit excellent corrosion resistance, wear resistance, high thermal stability of the alloy phase, high strength-toughness, and have been reported to be suitable in low-density refractory and high temperature for the aerospace engine blades [12,13]. Other potential applications comprise tools and molds, corrosion-resistant coatings, gas storage, nuclear reactors, and structural applications, from cryogenic temperatures to high temperatures [14–16].

1.1.2 Eutectic High Entropy Alloys

Currently, one of the main challenges in HEAs investigation encompass the incapacity to reach both high ductility and strength in single-phase HEAs [17]. In this regard, FCC single-phase HEAs tend to exhibit high ductility, while BCC single-phase HEAs possess merely good strength [18,19].

To overcome the strength/ductility paradigm, the concept of eutectic high entropy alloys (EHEAs) was first introduced by Lu et al. [20]. In their seminal work, a non-equiatomic lamellar AlCoCrFeNi$_{2.1}$ EHEA was designed, consisting of a CoCrFe-rich L1$_2$ FCC phase, acting as a soft phase, and a AlNi-rich B2 BCC phase, reinforced by nanoprecipitates, and therefore acting as a hard phase. Resulting from microstructural phase transformation and mechanical behaviour of the dual phase EHEA at room temperatures and cryogenic temperatures, Gao et al. [21] detected a high density of mobile dislocations within the FCC phase, which resulted in further strengthening of the alloy during deformation. Lu et al. [22] tracked that no phase transitions occurred during deformation, suggesting that the balance between ductility and strength does not arise from a stress-induced phase transition.

Additionally, this composition benefit from good thermophysical properties, including the absence of a solidification temperature interval, induced by the eutectic reaction, thus hindering segregation and shrinkage cavities [20]. As a result, an advantageous castability is recorded, entrusting EHEAs with great potential for industrial applications, particularly in the gas storage, aerospace engines, and ship coatings [23].

1.2 Fusion Welding of High Entropy Alloys

Upon the emergence of HEAs, understanding of their thermomechanical processability is particularly important, both to ensure their weldability, as well to assess the complex mechanisms conducting the microstructural evolution across the welded joint and resulting mechanical behaviour [14]. Considering the wide range of available welding techniques, fusion-based welding is a widely used manufacturing technology, based on melting and solidification of material, to assembly complex-shaped structures and produce components in tailored materials.

The fusion-based welding heat input induces changes in the microstructure of the welded region, allowing the development of distinct regions. The metal adjacent to the welded region, the fusion zone (FZ), experiences the highest temperature, forming a molten pool. The shape and penetration of the FZ is dominated by the fluid flow and the heat transfer in the molten pool, such as convection, heat conduction and radiation. Surrounding the FZ is the heat affected zone (HAZ), characterized by grain growth, phase dissolution and precipitation. The non-isothermal temperature cycles experienced at different distances from the centre of the FZ causes a heterogeneous microstructure, resulting in localized brittleness or hardening. Finally, the base material (BM), encompass the region where the microstructure remains unchanged during the process, due to its distance from the weld centreline.

1.2.1 Gas Tungsten Arc Welding

Regarding the fusion welding techniques for HEAs, laser welding process has drawn special attention due to their minimal HAZ, distortion, and low heat input. However, given the high operational costs of this method, electric arc welding techniques emerge as a cost-effective alternative [24].

Gas tungsten arc welding (GTAW) is a process, shown schematically in Fig. 1.2, where coalescence of metals is originated by producing an electric arc between a non-consumable tungsten and the BM, thus generating the heat required for the melting and joining of two workpieces. An inert shielding gas, typically argon or helium, connected to a protective gas cylinder, is used to protect the tungsten electrode and the molten metal from oxidation and possible contamination. A filler material may be used between two different workpieces to promote a smooth chemical transition. The filler material is normally fed into the weld area as bare metal filler rod.

GTAW is mostly applied for joining thin sections of stainless steel and light metals, since it has relatively limited heat input, thus offering greater control of weld filler dilution. However, this technique has inherently low deposition rate. Therefore, excessive welding currents must be avoided to prevent

the melting of the tungsten electrode, potentially translating in formation of intermetallic compounds and generation of residual stresses in the welded joint [25].

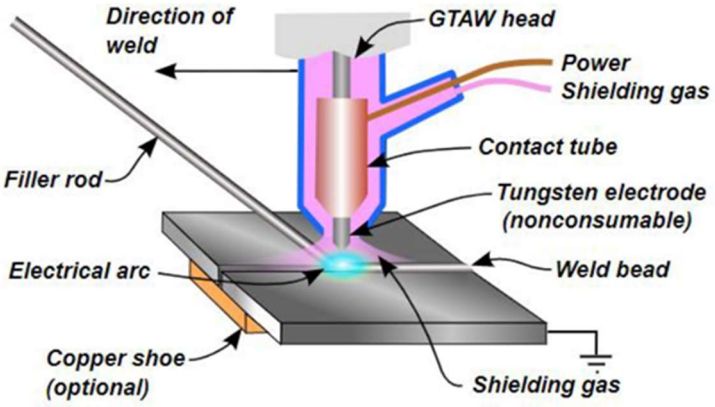

Figure 1.2 - Schematic illustration of GTAW process [26].

1.2.2 High Entropy Alloys Weldability

Currently, studies on HEAs weldability are expanding, revealing the primary focus has been devoted to assessing the weldability of the single-phase FCC Cantor Alloy CoCrFeMnNi. The existing literature details works on numerous welding techniques successfully applied to the CoCrFeMnNi alloy, such as GTAW [27], electron beam welding (EBW) [28], laser beam welding (LBW) [29], and friction stir welding (FSW) [30].

In this context, Oliveira et al. [27] studied the weldability of the cold-rolled CoCrFeMnNi alloy using the GTAW welding process. The results obtained revealed that the tensile strength and ductility of the FZ were lower than those of the BM, as a consequence of the large grain and pronounced material softening in the FZ. However, they were significantly higher when compared to weld joints produced by LBW for alloys with identical compositions, aligning with Wu et al. [31] research findings. The weld joints obtained in Oliveira's study exhibited full penetration and absence of defects, highlighting the potential weldability of this class of alloys.

1.2.3 Dissimilar Welding of High Entropy Alloys

The weldability of HEAs for structural applications may require dissimilar welding between different alloys, economically enabling the preparation of these structures and enhancing their potential [32]. However, dissimilar welding of materials with distinct microstructures, mechanical properties, and thermal conductivities arises a challenge in achieving viable joints, given the tendency for intermetallic compounds formation and microsegregation effects. Therefore, the selection of welding parameters and base material conditions is crucial to ensure the structural integrity of the joint.

Sokkalingam et al. studied the dissimilar welding between $Al_{0.1}$CoCrFeNi HEA and AISI 304 stainless steel, by GTAW [33] and EBW [34]. Both joints revealed evolution of columnar grains in the weld centerline area, while non-epitaxial grain growth occurred onto the AISI 304 side. The joint obtained from the GTAW recorded columnar to equiaxed grain transition. Conversely, the EBW joint only

evidenced columnar grains, attributed to the narrow weld bead size. The same group [35] further investigated the dissimilar welding between $Al_{0.1}$CoCrFeNi HEA and Inconel 718, using the GTAW welding process. The results indicated the $Al_{0.1}$CoCrFeNi HEA is favourable for dissimilar welding with Inconel 718, and a defect-free joint can be obtained. The microstructure analysis performed evidenced that the weld interface displayed columnar dendritic grains. However, the joint exhibited NbC/Laves phases segregation occurring at unmixed zones, promoting early crack initiation when submitted to residual strains.

1.2.4 Eutectic High Entropy Alloys Weldability

The study on the weldability of EHEAs is still in an early stage. As of now, solid-state welding techniques are the main methods used to join the AlCoCrFeNi$_{2.1}$ EHEA [36,37]. Considerable effort has gone into address the weldability of this novel engineering alloys via fusion welding. Recently, Zhang et al. [38] attempted joining EHEAs via LBW, achieving a defect-free fully penetrated joint. However, the investigation of AlCoCrFeNi$_{2.1}$ EHEA joining via a cost-effective fusion welding technique is still lacking comprehensive understanding.

Shen at al. [39] bridge this gap by studying the effect of the GTAW welding process on the microstructure and mechanical properties of an as-cast AlCoCrFeNi$_{2.1}$ EHEA. The mechanical tests performed evidenced a higher yield strength of the joints, comparing to the base material, due to the greater cooling rate imposed during solidification. During the rapid cooling rate, it was observed the grains assumed the growing directions (1 0 1) and (0 0 1) for the FCC and B2 BCC phase, respectively, coinciding with the reported in EHEAs [40]. In accordance with Xiong et al. [41], Shen et al. also recorded the lamellar structure of B2 BCC and FCC phases are strengthened by the dissolution of nanosized phases, leading to a pronounced softening in HAZ. The tensile strength and fracture strain, when failure occurred in the BM, was 1026 MPa and 13.0%, respectively. These results are consistent with the load transfer mechanism across the welded joint, suggesting that the dispersed nanosized particles in the soft HAZ allows to accommodate a greater deformation, ultimately attributed to the FCC and B2 BCC phase synergy between strength and ductility [39].

1.3 State of the Art

From the literature review, it is possible to conclude that extensive research and development over the past few years have allowed to further assess the weldability of these novel class of alloys, holding great promise for structural applications. However, there are still relatively limited knowledge concerning the dissimilar welding of the AlCoCrFeNi$_{2.1}$ EHEA to traditional metals, hindering the assessment of welding conditions, microstructure and mechanical behaviour synergy. Therefore, the dissimilar welding of EHEAs must be deeply investigated to pave the way for potential engineering applications.

2

MATERIALS AND METHODS

2.1 Materials

In this study, two different 1.5 mm thick dissimilar sheet combinations were prepared: one as-cast $AlCoCrFeNi_{2.1}$ EHEA/316 stainless steel with dimension of 67 mm x 51 mm x 1.5 mm (length x width x thickness), and other as-cast $AlCoCrFeNi_{2.1}$ EHEA/Inconel 718 with dimensions of 88 mm x 64 mm x 1.5 mm. The as-cast $AlCoCrFeNi_{2.1}$ EHEA was fabricated by employing vacuum induction melting and ingot casting, as described in [39]. For reference, the compositions of the three BMs used (in aspect ratio of at. %) are provided in Table 1.

Table 1 - Chemical composition (in aspect ratio of at. %) of the base materials used in the samples.

Composition (at. %)	Al	Co	Cr	Fe	Ni	Nb	C	Si	Mn	Mo	Cu	N	P	S
$AlCoCrFeNi_{2.1}$	16.39	16.39	16.39	16.39	34.43	–	–	–	–	–	–	–	–	–
316 Stainless Steel	–	–	16.20	–	11.00	–	0.02	0.50	1.71	2.18	0.30	0.35	0.07	0.02
Inconel 718	–	–	22.50	19.80	54.50	2.80	–	–	–	–	–	–	–	–

Prior to welding, preliminary tests were performed on 1.5 mm thick 316 stainless steel sheets, thus allowing the selection of optimal process parameters for the achievement of full penetration and avoiding possible welding defects. The outer oxide layer of the base materials was carefully removed with 1200 grit SiC paper. Then, alcohol and ethanol were employed to clean the samples and prevent possible impurities on the joining surfaces.

2.2 Methods

2.2.1 Gas Tungsten Arc Welding

GTAW was performed using an *OERLIKON*, model *CITOTIG 2200 Force* equipment, coupled with an in-house custom-made computer numerical control (CNC) machine used to control the movement of the platform where the samples were placed. The welding parameters resulting from the process optimization are listed in Table 1.

Table 2 - Process parameters for the dissimilar welding of the $AlCoCrFeNi_{2.1}$ EHEA with 316 stainless steel / Inconel 718

Current [A]	Voltage [V]	Travel Speed [mm/s]	Gas Flow Rate [L/min]	Heat Input [J/mm]
65	12.6	2	14	409.5

The tip of the non-consumable tungsten electrode was positioned slightly towards the $AlCoCrFeNi_{2.1}$ EHEA BM, at a constant distance of 1.5 mm from the samples. Throughout the welding process 99.99% pure Argon shielding gas was supplied through the nozzle and the platform at a constant flow rate, to prevent the molten pool and its surroundings from oxidation. The obtained samples are depicted in Fig. 2.1.

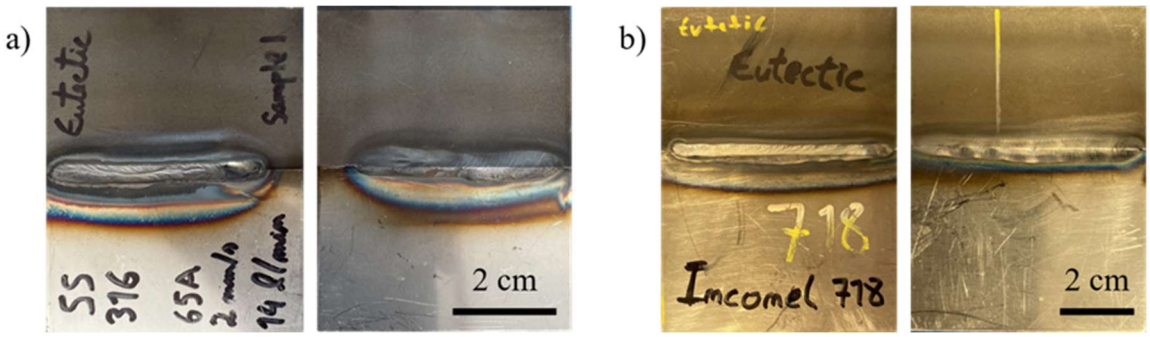

Figure 2.1 - Final Dissimilar welded joints: a) $AlCoCrFeNi_{2.1}$ EHEA / 316 stainless steel, b) $AlCoCrFeNi_{2.1}$ EHEA / Inconel 718

2.2.2 Microstructural Analysis

To perform the microstructural analysis of the distinct regions of the welded joints, conventional specimen preparation for optical metallography was carried out. Initially, the samples were cut by electrical discharge machine, followed by mounting of the representative cross-section with epoxy resin. The samples were then mechanically polished, using a *MINITECH 333 - PRESI* polishing machine, with silicon carbide sandpapers in these steps: 320, 400, 600, 800, 1000, 1200, 2500 and 4000 grit. After 4000 grit the samples were polished with a 3 µm diamond compound and a polish cloth until a reflecting surface was observable. Afterwards, the different regions of the weld were contrasted with aqua regia solution, which was composed of HNO_3 and HCl, combined at 1:3 ratio in volume, respectively.

Lastly, *Leica DMI5000 M* inverted optical microscope was used to analyze the dissimilar joints cross section microstructures.

2.2.3 Mechanical Analysis

To further analyse the influence of the weld thermal cycles across the welded joints, conventional microhardness measurements were conducted throughout the transversal section of the joints, using a *Zwick Roell ZHV1-M* Vickers hardness tester. During the indentation process, a 500 g load, kept during 10 s, was applied. The space between consecutive indents was kept at 150 μm, both horizontally and vertically, thus allowing to create a bi-dimensional microhardness map.

The tensile tests until fracture were performed in an *Autograph Shimadzu AG-50kNG* machine, in order to evaluate the strength and ductility of the welded joints. Finally, after the fracture of the joints, scanning electron microscopy (SEM) was employed to assess the fracture surfaces, using a *Hitachi SU3800* machine.

3

RESULTS AND DISCUSSION

3.1 Optical Microscopy

To analyse the microstructure of the different welded regions, an optical micrography was performed. Fig. 3.1 depicts the macroscopic and microstructural features of the dissimilar welded joint composed of a $AlCoCrFeNi_{2.1}$ EHEA and a commercially available 316 stainless steel, detailing the effect of the weld thermal cycle across the joint. From the macroscopic morphology of the cross-section, presented in Fig. 3.1, it can be observed a full penetration and defect-free joint, with no pores or cracking. The FZ boundary is delineated by black dashed lines, to provide a clearer perspective on the microstructural differences across the joint.

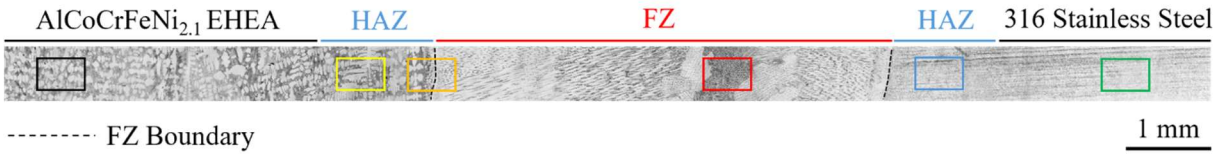

Figure 3.1 - Overview of the optical microscopy performed on the $AlCoCrFeNi_{2.1}$ EHEA/316 stainless steel dissimilar welded joint cross-section.

The $AlCoCrFeNi_{2.1}$ EHEA BM microstructure is detailed in Fig. 3.2 a). Although the BM originated from the same ingot as in [39], a fully lamellar eutectic microstructure was not observed. Instead, a dendritic microstructure, composed of a FCC primary phase, and a FCC + B2 BCC eutectic constituent was evidenced, as indicated with an array in Fig. 3.2 a). The different microstructure observed disclose a localized deviation from the eutectic composition, similar to that reported by Lopes et al. [42]. This can be mainly attributed to non-equilibrium solidification conditions that distinct parts of the ingot underwent, resulting in a heterogeneous structure throughout different regions. Moreover, literature reports suggest that the brighter and darker contrast regions, evidenced in the eutectic constituent, correspond to FCC and B2 BCC phases, respectively [43–45].

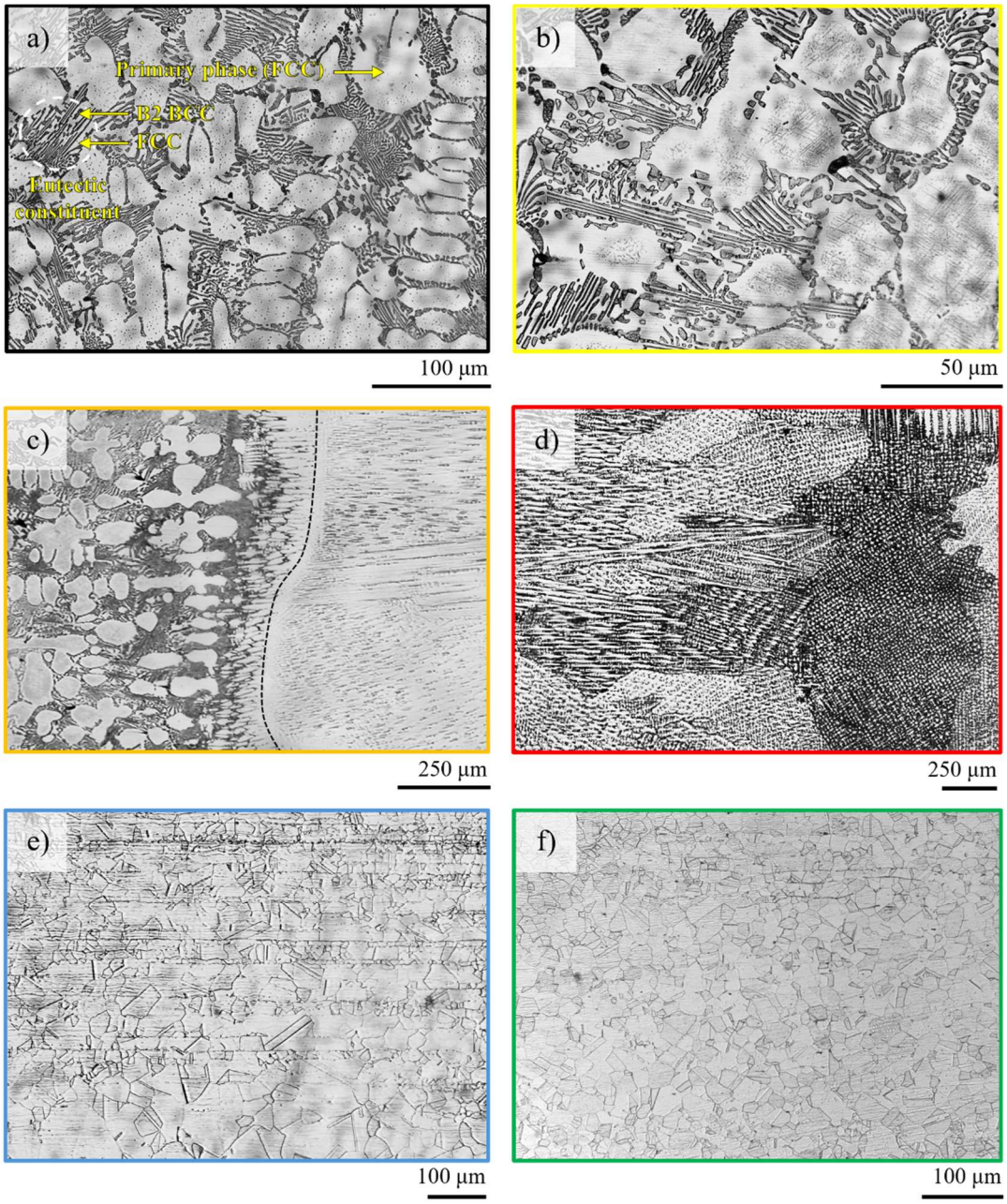

Figure 3.2 - Close up views of the regions marked in Figure 3.1: a) $AlCoCrFeNi_{2.1}$ EHEA BM; b) $AlCoCrFeNi_{2.1}$ EHEA HAZ; c) $AlCoCrFeNi_{2.1}$ EHEA FZ boundary; d) FZ; e) 316 stainless steel HAZ; f) 316 stainless steel BM.

Adjacent to the BM, the presence of the $AlCoCrFeNi_{2.1}$ EHEA HAZ can be identified, as shown with Fig. 3.2 b). Analysis of the HAZ reveals that the effects of weld thermal cycles and grain recrystallization are not clearly distinguished, as no obvious coarsening of the grains was detected. This can be related to both by the characteristic dendritic structure of the BM, which hinders grain growth detection, and by the strong diffusion requirement of atoms to accomplish the migration of grain boundaries [46]. Overall, HAZ reveals a similar morphology to that of the BM.

Towards the FZ boundary, where the temperature is higher and the solid grains are in contact with the melted material, significant changes in the joint microstructure were observed, as depicted in Fig. 3.2 c). A refinement, coupled with a modification in grain morphology from large dendrites

encompassing the FCC primary phase and eutectic constituent to a refined dendritic grain structure, was detected. This contrast in grain morphology can possibly be related with the permanence time at high temperatures at the solid/liquid interface, evidencing the effect of the cooling rate on the solidification microstructure. Additionally, these grains seem to have aligned to the favourable growth direction, perpendicular to the FZ boundary. The current observations are coherent with the solidification theory of metals, where grain growth is reported to occur along the parallel direction to that of the maximum temperature gradient at the molten pool boundary [47,48].

Immediately after the FZ boundary, it is possible to observe a rather large FZ, in Fig. 3.2 d), which experiences the peak-temperature, mixing of the two BMs, and a rapid non-equilibrium solidification, promoted by the colder HAZ. The substantial amount of melted material, combined with the large width of this region, generates an increase in the cooling rate, as reported previously for the arc welding processes [27]. Here the absence of homogeneity of grain morphologies is evidenced, varying from equiaxial dendritic structures to coarse elongated dendritic structures dispersed amongst the melt pool, resulting from the fluid flow conditions as the welding torch progressively shifts position. The emergence of new dendritic structures provides new nucleation spots for the liquid solidification, promoting growth rate. This is coherent with previous reports, where these elongated coarse grains tend to arise from competitive growth, emerging as dendritic structures [49].

Fig. 3.2 e) and f) depict the 316 stainless steel HAZ and BM, respectively. Contrasting with the dendritic microstructures of the previous regions, here an austenitic structure consisting of equiaxed grains was evidenced. It was also observed a slightly more refined grain structure from the HAZ, comparing to the BM, aided by the weld thermal cycles. Thus, a strengthening increment is induced at this location [50].

The dissimilar welded joint composed of a $AlCoCrFeNi_{2.1}$ EHEA and Inconel 718 is also found to exhibit full penetration and an absence of welding defects, as depicted in the macroscopic morphology of the cross-section in Fig. 3.3, indicating the promising weldability for engineering applications of the $AlCoCrFeNi_{2.1}$ EHEA/Inconel 718 pair, using the GTAW process.

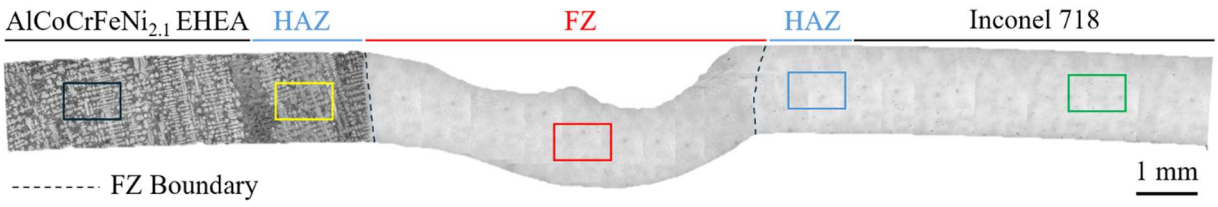

Figure 3.3 - Overview of the optical microscopy performed on the $AlCoCrFeNi_{2.1}$ EHEA/ Inconel 718 welded joint cross-section.

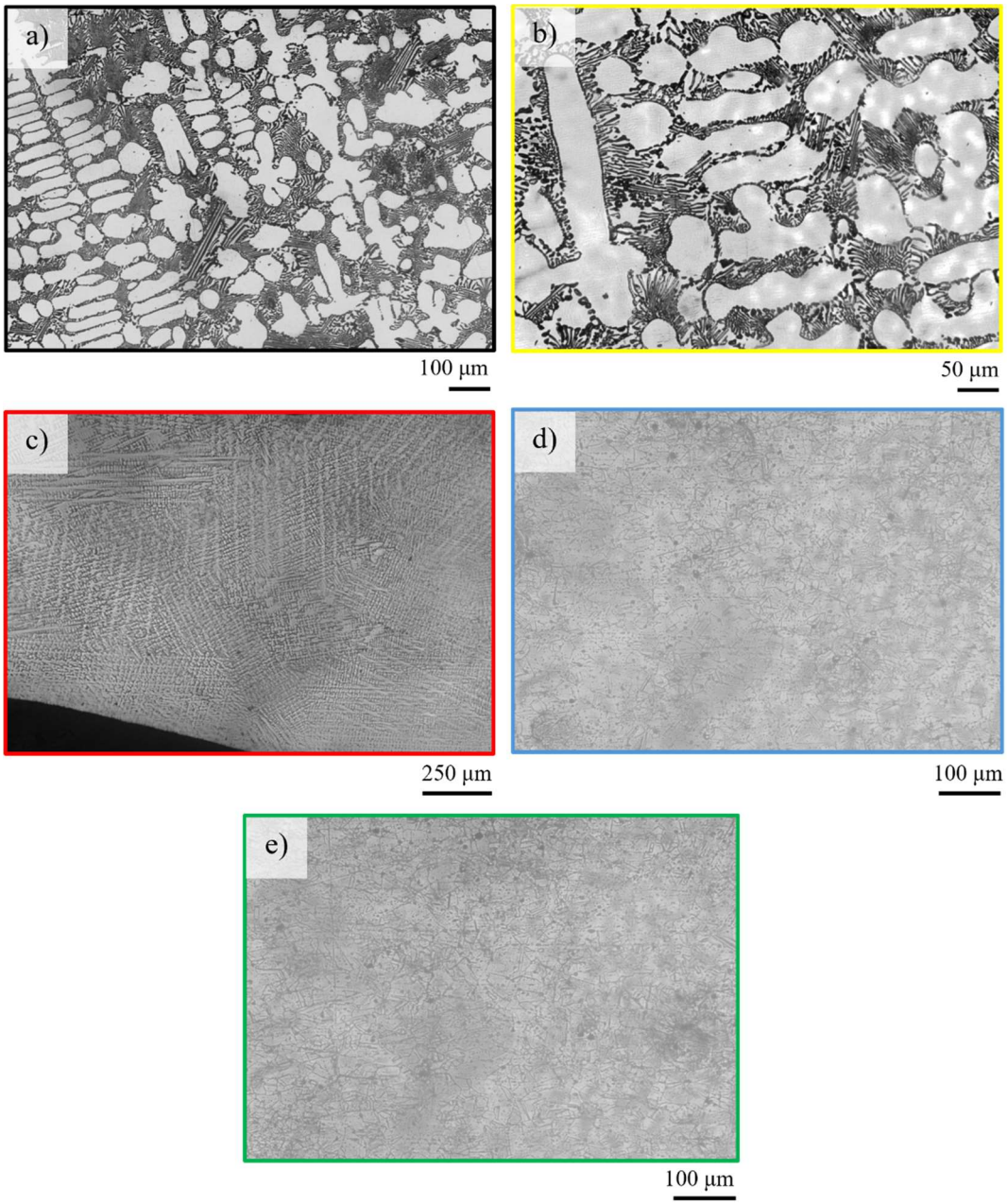

Figure 3.4 - Close up views of the regions marked in Figure 3.3: a) $AlCoCrFeNi_{2.1}$ EHEA BM; b) $AlCoCrFeNi_{2.1}$ EHEA HAZ; c) FZ; d) Inconel 718 HAZ; e) Inconel 718 BM.

Overall, it was observed that the microstructures in the $AlCoCrFeNi_{2.1}$ EHEA BM and HAZ, shown in Fig. 3.4 a) and b) respectively, were similar to the previous joint since the same welding parameters were employed. However, the FZ, depicted in Fig. 3.4 c), evidences a slight decrease in both the occurrence of coarse elongated dendritic structures and grain size, although a similar grain morphology is showcased. This microstructural variation can be explained by the different material thermophysical properties composing the joints, thus promoting distinct solidification conditions in this region [51].

Delving into the Inconel 718 HAZ and BM, an austenitic microstructure was displayed, as noticeable in Fig. 3.4 d) and e). Moreover, although the grain size was not completely uniform, grain coarsening in the HAZ, compared to those in the BM was almost negligible. This was influenced by the

Inconel 718 excellent heat resistance and strength at elevated temperatures, and thus the heat input influence on this region was not pronounced [52].

3.2 Microhardness Measurements

To further analyse the effect of variation in grain size and weld thermal cycles across the dissimilar joints, and therefore assess the resulting mechanical properties, microhardness measurements were carried out through the different zones of the joint.

Fig. 3.5 a) details the microhardness map throughout the $AlCoCrFeNi_{2.1}$ EHEA/316 stainless steel dissimilar welded joint, while Fig. 3.5 b) shows the extracted microhardness profile evolution at mid height of the weld. Six distinct regions are identified. The $AlCoCrFeNi_{2.1}$ EHEA BM (region 1) comprises the highest average hardness across the whole joint (≈310 HV), as expected. However, it is important to mention that the region 1 evidenced slightly lower hardness values than that observed in [42], which is possibly associated with the part from where the BM sheet was extracted from the ingot.

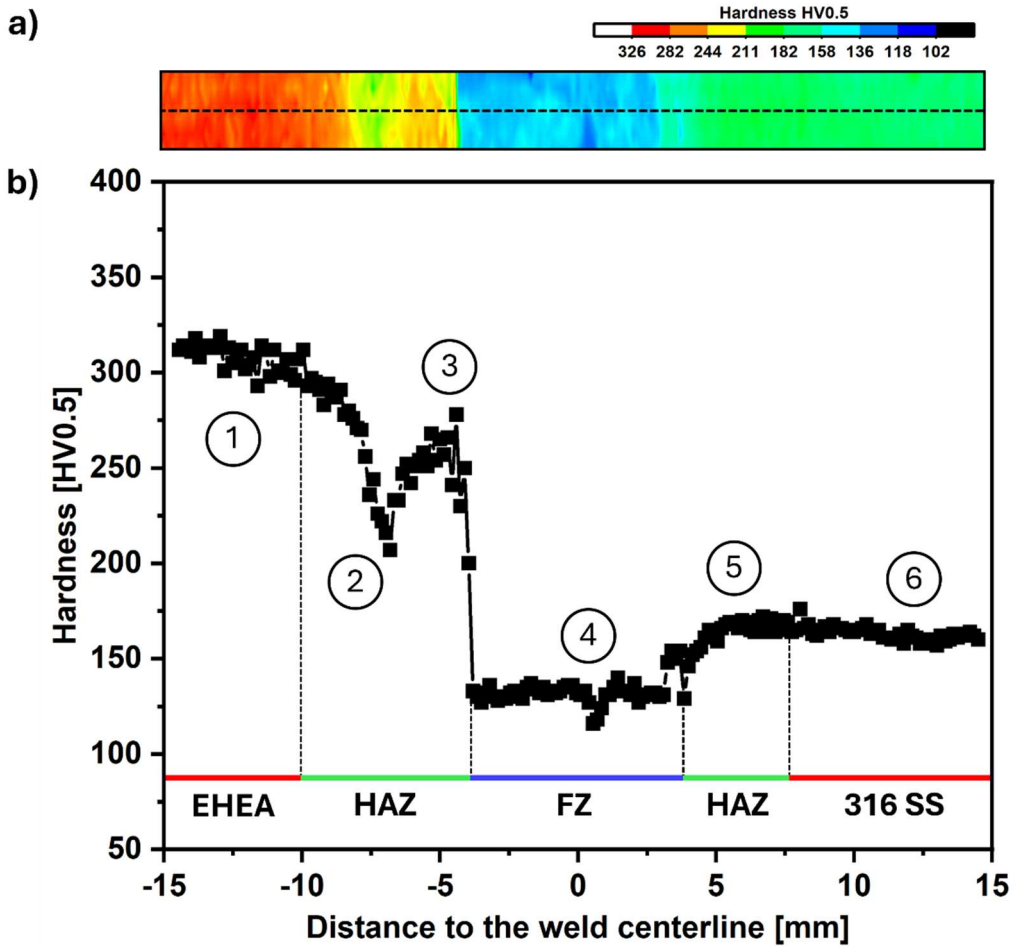

Figure 3.5 - a) Microhardness color map across the $AlCoCrFeNi_{2.1}$ EHEA/316 stainless steel dissimilar welded joint; b) Microhard-ness profile obtained at mid height of the welded joint.

Moving to the HAZ (region 2), a decreasing trend in hardness value is observed, reaching its lowest value at ≈210 HV. Although a similar microstructure morphology was observed in the previous optical micrography, compared to the BM, the evidenced drop in hardness can be traced to the decrease of nanoprecipitates in the eutectic constituent. Previously, Xiong et al. [41] and Shen et al. [39] pointed out that the presence of nanoprecipitates on the FCC and B2 BCC phases effectively induces a strengthening effect on a similar dual-phase EHEA. Thus, it is possible to deduce that the volume fraction reduction of the nanoprecipitates in this region, as verified by Shen et al., will generate a softening effect. Towards the FZ, but still in the HAZ (region 3), a hardness increase from ≈210 HV to ≈270 HV is detected, attributed to the refined dendritic grain structure inherent to this region, as confirmed by the optical microscopy images. Additionally, Shen et al. [39] further suggests that these increased hardness values can be explained by the segregation of the Cr element, occurring near the molten pool, within the B2 BCC precipitates.

Region 4 comprises the FZ, where a sharp decrease from the hardness values is recorded (from ≈270 HV to ≈130 HV). Previous reports in the literature evidenced an increment in the FZ measured hardness promoted by the mechanism of solid solution strengthening, aided by the increase of carbon content on the molten pool during the fusion of the 316 stainless steel, which was not verified in the current work [50,51]. In fact, the measured values are most likely correlated with the coarse elongated dendritic structures formed during the rapid non-equilibrium solidification. Therefore, the increase in grain size translates into fewer grain boundaries, which are generally considered to function as stationary impediments for gliding dislocations, resulting in lower hardness values. Such behaviour is compliant with the Hall-Petch effect.

From region 5, it may be noted a hardness increase to ≈175 HV, followed by a slight decrease to ≈160 HV transitioning from the 316 stainless steel HAZ to the BM, as detailed in region 6. This can be explained by the exposure to weld thermal cycles for extended durations, inducing recrystallization effects and consequently reducing grain size.

Fig. 3.6 shows the microhardness map and profile evolution along the $AlCoCrFeNi_{2.1}$ EHEA/Inconel 718 dissimilar welded joint. Region 1 measured values are consistent with the previously analysed joint. However, in region 2, a slight hardness increase (from ≈310 HV to ≈325 HV) was observed, indicating a more pronounced recrystallization effect occurred close to the BM. As progression towards the FZ boundary continues, a similar hardness evolution is registered compared to the previous joint, comprising a hardness decay to ≈210 HV, followed by a clear upward trend.

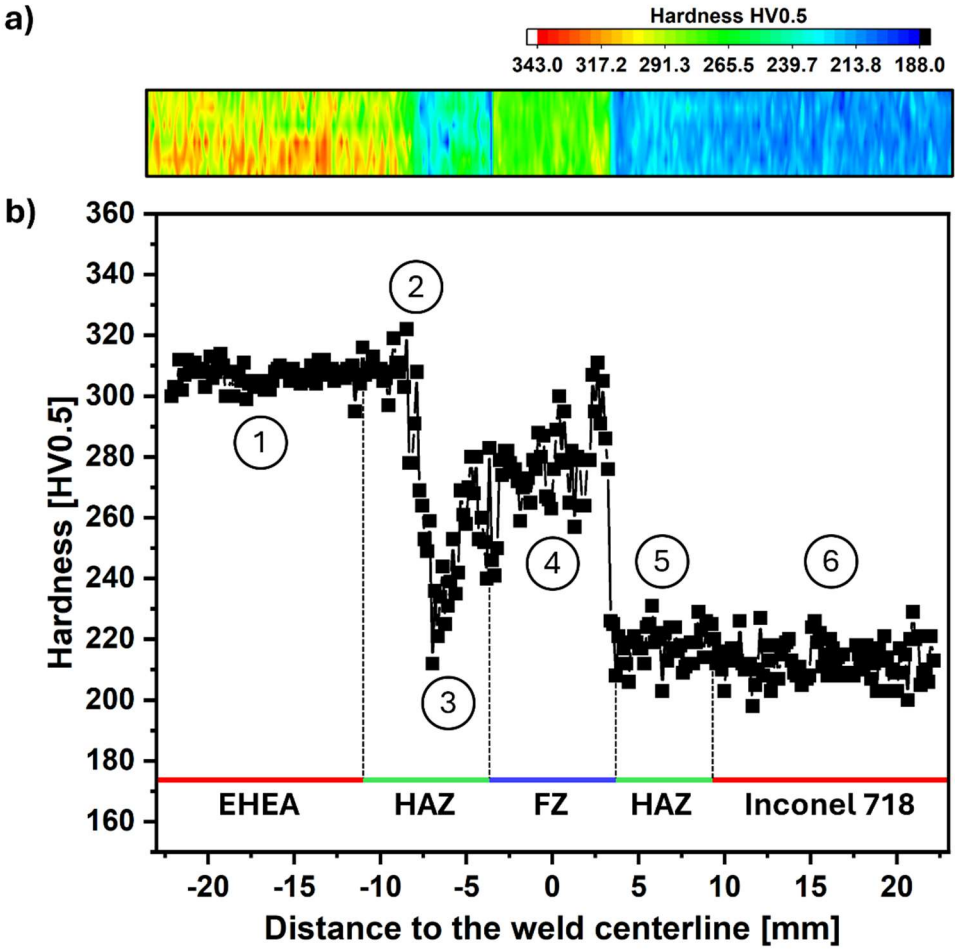

Figure 3.6 – a) Microhardness color map across the AlCoCrFeNi$_{2.1}$ EHEA/Inconel 718 dissimilar welded joint; b) Microhardness pro-file obtained at mid height of the welded joint.

Upon reaching the FZ (region 4), interestingly, an opposite behaviour is observed, marked by an increase in hardness values to an average of ≈280 HV, which likely corresponds to the decrease in the occurrence of coarse elongated dendritic structures in this region, comparing to the AlCoCrFeNi$_{2.1}$ EHEA/316 stainless steel welded joint. Moreover, it can also be perceived that the merging of these two BM induced a more prominent solid solution strengthening phenomena. In fact, Inconel 718 is a Ni-based superalloy widely recognized for its solid solution strengthening mechanisms, thus elucidating the evidenced hardness increment [53]. Sokkalingam et al. [35] also reported an increase in hardness values in the FZ corresponding to the perceived existence of NbC precipitates, commonly formed upon fusion of Inconel 718, corroborating the present discussion. Additionally, Oliveira et al. [51] further suggests the wide range of hardness values comprising the FZ (from ≈240 HV to ≈310 HV) can be explained by the asymmetrical chemical composition across this region. This phenomenon is directly linked to the Marangoni effect, where the rapid non equilibrium solidification, aided by the GTAW process, and the concentrations of dissimilar BMs will promote a complicated fluid flow, resulting in heterogeneous microsegregation along the FZ. However, it should be noted that to verify the asymmetrical chemical composition across the FZ, high energy synchrotron X-ray diffraction (XRD) or energy

dispersive X-ray spectroscopy (EDS) characterization techniques should be carried out, which was not possible in the current work.

Finally, regions 5 and 6 represent the HAZ and BM of the Inconel 718, respectively. Here, the average hardness values remained constant along both regions (≈215 HV), despite the disparity in the measured values, induced by the slight discrepancy in grain size, as previously reported in the optical micrography analysis.

3.3 Uniaxial Tensile Tests

To further analyse the synergy between the microstructural and mechanical features of the dissimilar joints, tensile tests until fracture at room temperature were performed. The mechanical properties of the fabricated base materials, namely ultimate tensile strength (σ_u) and fracture strain (ε_f), reported from the literature, are presented in Table 2 [39,54,55]. Comparing the base materials, it can be perceived that the $AlCoCrFeNi_{2.1}$ EHEA exhibits a higher σ_u than both 316 stainless steel and Inconel 718, while simultaneously presenting a considerably lower ε_f.

Table 3 - Summary of the base materials mechanical properties.

Reference	Ultimate Tensile Strength (σ_u) [MPa]	Fracture Strain (ε_f) [%]
$AlCoCrFeNi_{2.1}$ EHEA	1039	20.6
316 Stainless Steel	580	50
Inconel 718	743	48.4

However, when analysing the comprehensive stress-strain curves for the welded joints, provided in Fig. 3.7, an overall poorer mechanical behaviour of the dissimilar joints, compared to the base materials, is evidenced. The results are summarized in Table 3. The decrease in σ_u (432 MPa) and ε_f (9.7 %) in the $AlCoCrFeNi_{2.1}$ EHEA/316 stainless steel dissimilar welded joint can be mainly attributed to the heterogeneous and unfavourable microstructure in the FZ, where the fracture occurred. The equiaxial and coarse elongated dendritic structures dispersed amongst the FZ effectively induces complex tensile deformations, as previously reported by Mortezaie et al. [56] and Jo et al. [57], in dissimilar and similar joints, respectively. Moreover, it is well established in the literature that the coarse elongated grain structures are particularly susceptible to crack occurrence, triggering localized and preferential stress concentrations. This susceptibility arises both from the decreased grain boundary density inherent to this grain morphology structure, in comparison with the surrounding zones of the weld, and from the easier crack propagation path compared to the equiaxial grains [33,51]. Additionally, the reported loss in ductility can be traced to the broader heat distribution and subsequent larger FZ typical of GTAW processes, thus generating residual stresses upon the rapid non-equilibrium solidification [33]. These results are coherent with the previous microhardness measurements, considering: i) the strain concentration and subsequent fracture were accommodated in the lower hardness region (soft region); and ii)

the significantly high average hardness difference between the base materials (≈135 HV), thus elucidating the discrepancy in their mechanical behaviour.

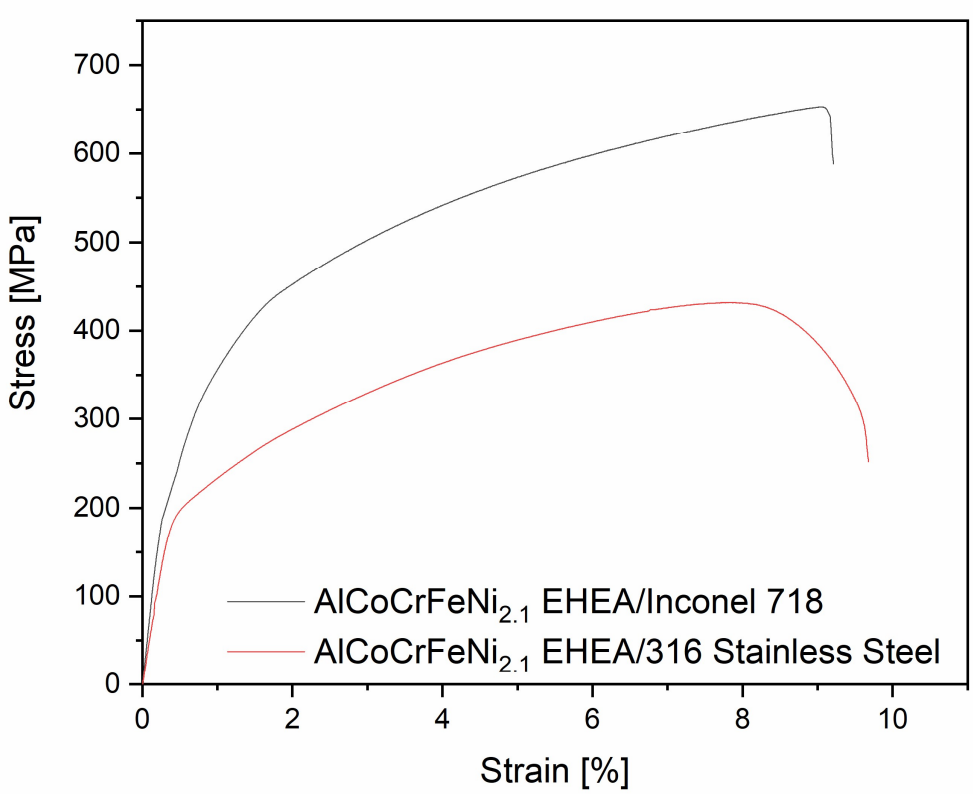

Figure 3.7 - Representative uniaxial test stress-strain curves for the AlCoCrFeNi$_{2.1}$ EHEA/316 stainless steel and AlCoCrFeNi$_{2.1}$ EHEA/Inconel 718 dissimilar welded joints.

Remarkably, the AlCoCrFeNi$_{2.1}$ EHEA/Inconel 718 dissimilar welded joint achieved a considerably higher σ_u (653 MPa) than that of the previous joint, with an almost negligible decrease in ε_f (9.2 %). The overall better mechanical features of this joint are most likely attributed to the solid solution strengthening previously reported. A similar phenomenon has also been observed by Afonso et al. [55] for a CoCrFeMnNi/Inconel 718 dissimilar welded joint, where the occurrence of Laves phases and orthorhombic phases (δ) (containing high concentrations of Ni and Nb) in the FZ, deriving from the Inconel 718, further promoted the enhancement of this phenomena. In fact, the Nb precipitates are generally located alongside the grains limit, effectively contributing to hinder the grains boundaries migration and promote lattice distortion effects, hence increasing the joint's σ_u. The lattice distortion effects can be elucidated by the Nb higher atomic radius [55,58]. Despite the less performing welded joints obtained in this study, compared to their respective base materials, it is worthy to note that they still present great potential for structural applications.

Table 4 - Summary of the welded joints mechanical properties.

Reference	Ultimate Tensile Strength (σ_u) [MPa]	Fracture Strain (ε_f) [%]
$AlCoCrFeNi_{2.1}$ EHEA/316 Stainless Steel	432	9.7
$AlCoCrFeNi_{2.1}$ EHEA/Inconel 718	653	9.2

3.4 Fracture Surfaces Analysis

Analysing the fracture surface analysis of the fractured tensile specimens can effectively provide insights on the fracture mechanism that occurred on the welded joints. Therefore, SEM was performed to visualize the fracture surfaces.

Fig. 3.8 illustrates the SEM fracture surface image of the $AlCoCrFeNi_{2.1}$ EHEA/316 stainless steel dissimilar welded joint. The several dimples distributed along the surface are in accordance with the considerably high plastic deformation experienced by the specimen, thus suggesting a ductile-like fracture mechanism occurred on this joint. Similar results have also been observed by Sokkalingam et al. [33]. In Fig. 3.8 b) is provided a closer view to the dimples formed during the plastic deformation and subsequent stretching and necking of the material, promoting the formation and propagation of fissures upon the dimples expansion and merging between themselves, under high levels of stress concentrations.

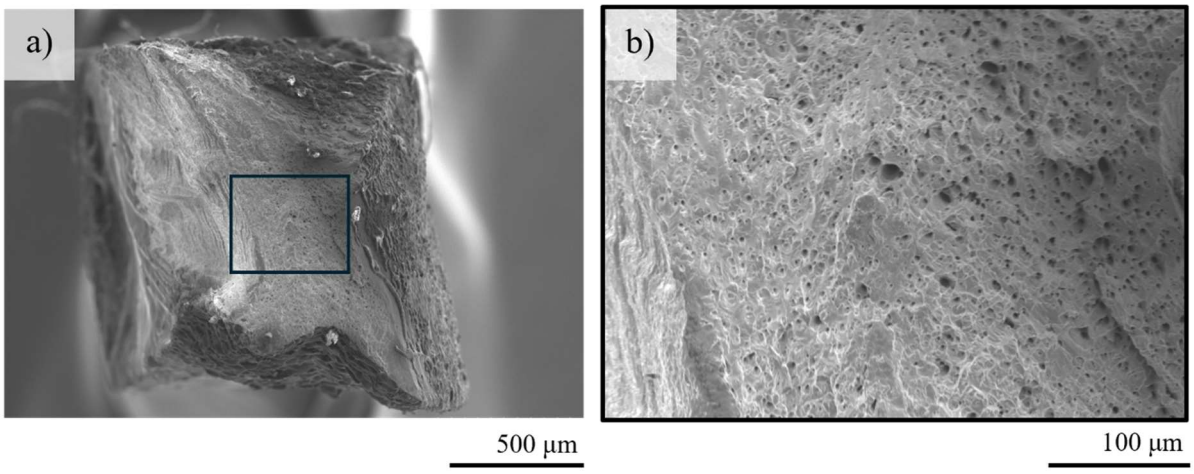

Figure 3.8 - SEM fractographs of the fracture surface of the AlCoCrFeNi2.1 EHEA/316 stainless steel specimens after the tensile test: a) Overview; b) Close up views of the region marked in a).

Concerning the $AlCoCrFeNi_{2.1}$ EHEA/Inconel 718 dissimilar welded joint, nickel-chromium-based superalloys are generally associated with ductile-like fracture mechanisms, while, on the other hand, $AlCoCrFeNi_{2.1}$ EHEAs have been reported to evidence a mixed of ductile and brittle fracture behaviour, ascribed to the brittle B2 BCC phase and the softer FCC phase [39,42,59,60]. In fact, Fig. 3.9 presents a faceted appearance, characteristic of a brittle-like fracture, along with the presence of dimples, although less frequent compared to the previous joint, thus indicating a mixed behaviour of

ductile and brittle fracture mechanisms took place on this welded joint. Afonso et al. [55] analysed the influence of intermetallic phases on the fracture behaviour and reported that the occurrence of Laves phase, formed upon the last stages of Inconel 718 melting and welded joint solidification, accounts for an incremental enhancement in joint embrittlement.

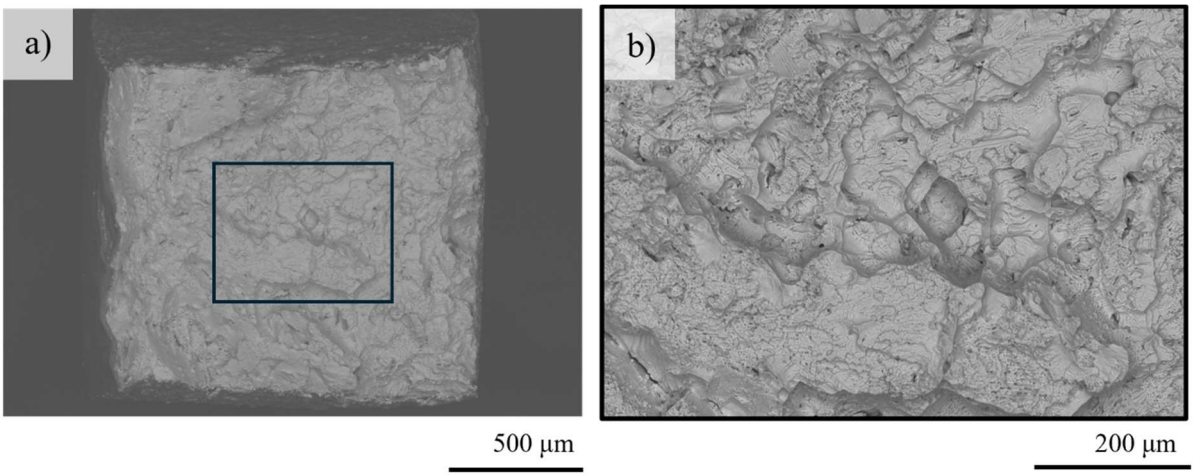

Figure 3.9 - SEM fractographs of the fracture surface of the $AlCoCrFeNi_{2.1}$ EHEA/ Inconel 718 specimens after the tensile test: a) Overview; b) Close up views of the region marked in a).

4

CONCLUSIONS AND FUTURE WORK

In this study, dissimilar welding of a $AlCoCrFeNi_{2.1}$ EHEA to 316 stainless steel and Inconel 718 by employing gas tungsten arc welding was performed. The effects of welding on this dissimilar joint's performance were investigated by establishing a comprehensive correlation between the joint's microstructural and mechanical properties. The most relevant findings from this study can be drawn:

- Overall, dissimilar GTAW of $AlCoCrFeNi_{2.1}$ EHEA to 316 stainless steel and Inconel 718 was successfully accomplished, without observable welding defects, evidencing the notable capability of this arc welding process to join these novel class of alloys to traditional metals.
- Optical microscopy analysis allowed to identify the effects of the thermal cycles and grain size fluctuations across the dissimilar welded joints. In particular, microstructural differences between the $AlCoCrFeNi_{2.1}$ EHEA BM and HAZ of both samples were not pronounced, whereas on the FZ a distinct grain morphology was evidenced, varying from equiaxial dendritic to coarse elongated dendritic structures, ultimately impacting the mechanical performance.
- Considering the microhardness mapping along the different regions of the welded joint, the $AlCoCrFeNi_{2.1}$ EHEA/316 stainless steel joint achieved the highest value in the $AlCoCrFeNi_{2.1}$ EHEA BM, while the lowest value was observed in the FZ. Conversely, the $AlCoCrFeNi_{2.1}$ EHEA/Inconel 718 joint registered significantly higher hardness values across the FZ, revealing a more prominent solid solution strengthening effect induced by the Inconel 718.
- Tensile tests evidenced a reduction in mechanical performance of the dissimilar welded joints, compared to their respective BMs, but still present great potential for industrial applications, due to their strength and ductility synergy. Overall, the $AlCoCrFeNi_{2.1}$ EHEA/Inconel 718 joint evidenced a superior strength and a slightly lower ductility ($\sigma_u \approx 653$ MPA and $\varepsilon_f \approx 9.2$ %) than that of the $AlCoCrFeNi_{2.1}$ EHEA/316 stainless steel joint ($\sigma_u \approx 432$ MPA and $\varepsilon_f \approx 9.7$ %).
- The fracture surface analysis revealed a ductile-like fracture behaviour from the $AlCoCrFeNi_{2.1}$ EHEA/316 stainless steel joint, whereas the $AlCoCrFeNi_{2.1}$ EHEA/Inconel 718 presented a mixed behaviour of ductile and brittle fracture mechanisms.

Looking forward, based on the study performed, additional experiments can be conducted to further assess the current research:

- Electron microscopy to complement the microstructure evolution across the welded joints.
- Electron backscatter diffraction (EBSD) to analyse the crystallographic texture along the joints.
- EDS and XRD to detect the occurrence of undesirable and detrimental phases on the molten pool.

- Thermodynamic calculations, following the Scheil model, and thus predicting the solidification behaviour throughout the rapid cooling of the FZ.
- Digital image correlation (DIC) and cycling tests to analyse the mechanical behaviour across different regions and the functional fatigue of the welded joint, respectively.
- Study the incorporation of nanopowders in the $AlCoCrFeNi_{2.1}$ EHEA/Inconel 718 joint to control and modulate the FZ microstructure.

BIBLIOGRAPHY

[1] J.W. Yeh, S.K. Chen, S.J. Lin, J.Y. Gan, T.S. Chin, T.T. Shun, C.H. Tsau, S.Y. Chang, Nanostructured High-Entropy Alloys with Multiple Principal Elements: Novel Alloy Design Concepts and Outcomes, Adv Eng Mater 6 (2004) 299–303. https://doi.org/10.1002/ADEM.200300567.

[2] B. Cantor, I.T.H. Chang, P. Knight, A.J.B. Vincent, Microstructural development in equiatomic multicomponent alloys, Materials Science and Engineering: A 375–377 (2004) 213–218. https://doi.org/10.1016/J.MSEA.2003.10.257.

[3] Y. Zhang, T.T. Zuo, Z. Tang, M.C. Gao, K.A. Dahmen, P.K. Liaw, Z.P. Lu, Microstructures and properties of high-entropy alloys, Prog Mater Sci 61 (2014) 1–93. https://doi.org/10.1016/J.PMATSCI.2013.10.001.

[4] J.W. Yeh, Recent progress in high-entropy alloys, Annales de Chimie: Science Des Materiaux 31 (2006) 633–648. https://doi.org/10.3166/ACSM.31.633-648.

[5] Y.F. Ye, Q. Wang, J. Lu, C.T. Liu, Y. Yang, High-entropy alloy: challenges and prospects, Materials Today 19 (2016) 349–362. https://doi.org/10.1016/J.MATTOD.2015.11.026.

[6] L.M. Martyushev, V.D. Seleznev, Maximum entropy production principle in physics, chemistry and biology, Phys Rep 426 (2006) 1–45. https://doi.org/10.1016/J.PHYSREP.2005.12.001.

[7] Y. Zhang, Y.J. Zhou, J.P. Lin, G.L. Chen, P.K. Liaw, Solid-Solution Phase Formation Rules for Multi-component Alloys, Adv Eng Mater 10 (2008) 534–538. https://doi.org/10.1002/ADEM.200700240.

[8] R.S. Mishra, N. Kumar, M. Komarasamy, Lattice strain framework for plastic deformation in complex concentrated alloys including high entropy alloys, Materials Science and Technology 31 (2015) 1259–1263. https://doi.org/10.1179/1743284715Y.0000000050.

[9] Z. Li, S. Zhao, R.O. Ritchie, M.A. Meyers, Mechanical properties of high-entropy alloys with emphasis on face-centered cubic alloys, Prog Mater Sci 102 (2019) 296–345. https://doi.org/10.1016/J.PMATSCI.2018.12.003.

[10] S. Ranganathan, Alloyed pleasures: Multimetallic cocktails, (2003).

[11] M.H. Tsai, J.W. Yeh, High-Entropy Alloys: A Critical Review, Mater Res Lett 2 (2014) 107–123. https://doi.org/10.1080/21663831.2014.912690.

[12] S. Shukla, T. Wang, S. Cotton, R.S. Mishra, Hierarchical microstructure for improved fatigue properties in a eutectic high entropy alloy, Scr Mater 156 (2018) 105–109. https://doi.org/10.1016/J.SCRIPTAMAT.2018.07.022.

[13] M. Dada, P. Popoola, S. Adeosun, N. Mathe, M. Dada, P. Popoola, S. Adeosun, N. Mathe, High Entropy Alloys for Aerospace Applications, Aerodynamics (2019). https://doi.org/10.5772/INTECHOPEN.84982.

[14] J.G. Lopes, J.P. Oliveira, A Short Review on Welding and Joining of High Entropy Alloys, Metals 2020, Vol. 10, Page 212 10 (2020) 212. https://doi.org/10.3390/MET10020212.

[15] C. Shang, E. Axinte, J. Sun, X. Li, P. Li, J. Du, P. Qiao, Y. Wang, CoCrFeNi(W1 − xMox) high-entropy alloy coatings with excellent mechanical properties and corrosion resistance prepared by mechanical alloying and hot pressing sintering, Mater Des 117 (2017) 193–202. https://doi.org/10.1016/J.MATDES.2016.12.076.

[16] M. V. Klimova, A.O. Semenyuk, D.G. Shaysultanov, G.A. Salishchev, S. V. Zherebtsov, N.D. Stepanov, Effect of carbon on cryogenic tensile behavior of CoCrFeMnNi-type high entropy alloys, J Alloys Compd 811 (2019) 152000. https://doi.org/10.1016/J.JALLCOM.2019.152000.

[17] S. Guo, C. Ng, J. Lu, C.T. Liu, Effect of valence electron concentration on stability of fcc or bcc phase in high entropy alloys, J Appl Phys 109 (2011). https://doi.org/10.1063/1.3587228/984570.

[18] F. Otto, A. Dlouhý, C. Somsen, H. Bei, G. Eggeler, E.P. George, The influences of temperature and microstructure on the tensile properties of a CoCrFeMnNi high-entropy alloy, Acta Mater 61 (2013) 5743–5755. https://doi.org/10.1016/J.ACTAMAT.2013.06.018.

[19] O.N. Senkov, G.B. Wilks, D.B. Miracle, C.P. Chuang, P.K. Liaw, Refractory high-entropy alloys, Intermetallics (Barking) 18 (2010) 1758–1765. https://doi.org/10.1016/J.INTERMET.2010.05.014.

[20] Y. Lu, Y. Dong, S. Guo, L. Jiang, H. Kang, T. Wang, B. Wen, Z. Wang, J. Jie, Z. Cao, H. Ruan, T. Li, A Promising New Class of High-Temperature Alloys: Eutectic High-Entropy Alloys, Scientific Reports 2014 4:1 4 (2014) 1–5. https://doi.org/10.1038/srep06200.

[21] X. Gao, Y. Lu, B. Zhang, N. Liang, G. Wu, G. Sha, J. Liu, Y. Zhao, Microstructural origins of high strength and high ductility in an AlCoCrFeNi2.1 eutectic high-entropy alloy, Acta Mater 141 (2017) 59–66. https://doi.org/10.1016/J.ACTAMAT.2017.07.041.

[22] Y. Lu, X. Gao, L. Jiang, Z. Chen, T. Wang, J. Jie, H. Kang, Y. Zhang, S. Guo, H. Ruan, Y. Zhao, Z. Cao, T. Li, Directly cast bulk eutectic and near-eutectic high entropy alloys with balanced strength and ductility in a wide temperature range, Acta Mater 124 (2017) 143–150. https://doi.org/10.1016/J.ACTAMAT.2016.11.016.

[23] Y. Lu, Y. Dong, H. Jiang, Z. Wang, Z. Cao, S. Guo, T. Wang, T. Li, P.K. Liaw, Promising properties and future trend of eutectic high entropy alloys, Scr Mater 187 (2020) 202–209. https://doi.org/10.1016/J.SCRIPTAMAT.2020.06.022.

[24] J. Li, X. Meng, L. Wan, Y. Huang, Welding of high entropy alloys: Progresses, challenges and perspectives, J Manuf Process 68 (2021) 293–331. https://doi.org/10.1016/J.JMAPRO.2021.05.042.

[25] A.N. Chaudhari, K. Dixit, G.S. Bhatia, B. Singh, P. Singhal, K.K. Saxena, Welding Behaviour of Duplex Stainless Steel AISI 2205: AReview, Mater Today Proc 18 (2019) 2731–2737. https://doi.org/10.1016/J.MATPR.2019.07.136.

[26] R. Kumar, N.R. Mevada, S. Rathore, N. Agarwal, V. Rajput, A.S. Barad, Experimental Investigation and Optimization of TIG Welding Parameters on Aluminum 6061 Alloy Using Firefly Algorithm, IOP Conf Ser Mater Sci Eng 225 (2017) 012153. https://doi.org/10.1088/1757-899X/225/1/012153.

[27] J.P. Oliveira, T.M. Curado, Z. Zeng, J.G. Lopes, E. Rossinyol, J.M. Park, N. Schell, F.M. Braz Fernandes, H.S. Kim, Gas tungsten arc welding of as-rolled CrMnFeCoNi high entropy alloy, Mater Des 189 (2020) 108505. https://doi.org/10.1016/J.MATDES.2020.108505.

[28] M.G. Jo, H.J. Kim, M. Kang, P.P. Madakashira, E.S. Park, J.Y. Suh, D.I. Kim, S.T. Hong, H.N. Han, Microstructure and mechanical properties of friction stir welded and laser welded high entropy alloy CrMnFeCoNi, Metals and Materials International 24 (2018) 73–83. https://doi.org/10.1007/S12540-017-7248-X/METRICS.

[29] N. Kashaev, V. Ventzke, N. Stepanov, D. Shaysultanov, V. Sanin, S. Zherebtsov, Laser beam welding of a CoCrFeNiMn-type high entropy alloy produced by self-propagating high-temperature synthesis, Intermetallics (Barking) 96 (2018) 63–71. https://doi.org/10.1016/J.INTERMET.2018.02.014.

[30] H. Do, S. Asadi, N. Park, Microstructural and mechanical properties of dissimilar friction stir welded CoCrFeMnNi high entropy alloy to STS304 stainless steel, Materials Science and Engineering: A 840 (2022) 142979. https://doi.org/10.1016/J.MSEA.2022.142979.

[31] Z. Wu, S.A. David, D.N. Leonard, Z. Feng, H. Bei, Microstructures and mechanical properties of a welded CoCrFeMnNi high-entropy alloy, Science and Technology of Welding and Joining 23 (2018) 585–595. https://doi.org/10.1080/13621718.2018.1430114.

[32] C. Lin, R.K. Shiue, S.K. Wu, Y.S. Lin, Dissimilar Infrared Brazing of CoCrFe(Mn)Ni Equiatomic High Entropy Alloys and 316 Stainless Steel, Crystals 2019, Vol. 9, Page 518 9 (2019) 518. https://doi.org/10.3390/CRYST9100518.

[33] R. Sokkalingam, V. Muthupandi, K. Sivaprasad, K.G. Prashanth, Dissimilar welding of Al0.1CoCrFeNi high-entropy alloy and AISI304 stainless steel, J Mater Res 34 (2019) 2683–2694. https://doi.org/10.1557/JMR.2019.186.

[34] R. Sokkalingam, P. Mastanaiah, V. Muthupandi, K. Sivaprasad, K.G. Prashanth, Electron-beam welding of high-entropy alloy and stainless steel: microstructure and mechanical properties, Materials and Manufacturing Processes 35 (2020) 1885–1894. https://doi.org/10.1080/10426914.2020.1802045.

[35] R. Sokkalingam, B. Pravallika, K. Sivaprasad, V. Muthupandi, K.G. Prashanth, Dissimilar welding of high-entropy alloy to Inconel 718 superalloy for structural applications, J Mater Res 37 (2022) 272–283. https://doi.org/10.1557/S43578-021-00352-W/FIGURES/8.

[36] P. Li, S. Wang, Y. Xia, X. Hao, H. Dong, Diffusion bonding of AlCoCrFeNi2.1 eutectic high entropy alloy to TiAl alloy, J Mater Sci Technol 45 (2020) 59–69. https://doi.org/10.1016/J.JMST.2019.10.041.

[37] P. Li, H. Sun, S. Wang, X. Hao, H. Dong, Rotary friction welding of AlCoCrFeNi2.1 eutectic high entropy alloy, J Alloys Compd 814 (2020) 152322. https://doi.org/10.1016/J.JALLCOM.2019.152322.

[38] M. Zhang, D. Wang, L. He, X. Ye, W. Zhang, Laser beam welding of AlCoCrFeNi2.1 eutectic high-entropy alloy, Mater Lett 308 (2022) 131137. https://doi.org/10.1016/J.MATLET.2021.131137.

[39] J. Shen, P. Agrawal, T.A. Rodrigues, J.G. Lopes, N. Schell, Z. Zeng, R.S. Mishra, J.P. Oliveira, Gas tungsten arc welding of as-cast AlCoCrFeNi2.1 eutectic high entropy alloy, Mater Des 223 (2022) 111176. https://doi.org/10.1016/J.MATDES.2022.111176.

[40] Y. Zhu, S. Zhou, Z. Xiong, Y.J. Liang, Y. Xue, L. Wang, Enabling stronger eutectic high-entropy alloys with larger ductility by 3D printed directional lamellae, Addit Manuf 39 (2021) 101901. https://doi.org/10.1016/J.ADDMA.2021.101901.

[41] T. Xiong, S. Zheng, J. Pang, X. Ma, High-strength and high-ductility AlCoCrFeNi2.1 eutectic high-entropy alloy achieved via precipitation strengthening in a heterogeneous structure, Scr Mater 186 (2020) 336–340. https://doi.org/10.1016/J.SCRIPTAMAT.2020.04.035.

[42] J.G. Lopes, A. Candeias, P. Agrawal, J. Shen, N. Schell, R.S. Mishra, J.P. Oliveira, Role of TiB2 inoculation particles during welding of a AlCoCrFeNi high entropy alloy, J Alloys Compd 995 (2024) 174694. https://doi.org/10.1016/J.JALLCOM.2024.174694.

[43] P. Shi, W. Ren, T. Zheng, Z. Ren, X. Hou, J. Peng, P. Hu, Y. Gao, Y. Zhong, P.K. Liaw, Enhanced strength–ductility synergy in ultrafine-grained eutectic high-entropy alloys by inheriting microstructural lamellae, Nat Commun 10 (2019). https://doi.org/10.1038/S41467-019-08460-2.

[44] D. Choudhuri, S. Shukla, P.A. Jannotti, S. Muskeri, S. Mukherjee, J.T. Lloyd, R.S. Mishra, Characterization of as-cast microstructural heterogeneities and damage mechanisms in eutectic AlCoCrFeNi2.1 high entropy alloy, Mater Charact 158 (2019) 109955. https://doi.org/10.1016/J.MATCHAR.2019.109955.

[45] D. Choudhuri, P.A. Jannotti, S. Muskeri, S. Shukla, S. Gangireddy, S. Mukherjee, B.E. Schuster, J.T. Lloyd, R.S. Mishra, Ballistic Response of a FCC-B2 Eutectic AlCoCrFeNi2.1 High Entropy Alloy, Journal of Dynamic Behavior of Materials 5 (2019) 495–503. https://doi.org/10.1007/S40870-019-00220-Z.

[46] Y. Fukuda, Y. Kado, T. Yoshikawa, K. Oishi, Y. Mae, Diffusion distances of the constituent atoms in the metallurgical phenomena such as recovery, recrystallization, grain growth, and

aging in aluminum and copper alloys, J Mater Eng Perform 11 (2002) 544–550. https://doi.org/10.1361/105994902770343809/METRICS.

[47] T. Debroy, S.A. David, Physical processes in fusion welding, Rev Mod Phys 67 (1995) 85. https://doi.org/10.1103/RevModPhys.67.85.

[48] S.A. David, S.S. Babu, J.M. Vitek, Welding: Solidification and microstructure, JOM 55 (2003) 14–20. https://doi.org/10.1007/S11837-003-0134-7/METRICS.

[49] S. Suwas, R.K. Ray, Crystallographic Texture of Materials, (2014). https://doi.org/10.1007/978-1-4471-6314-5.

[50] J.P. Oliveira, J. Shen, Z. Zeng, J.M. Park, Y.T. Choi, N. Schell, E. Maawad, N. Zhou, H.S. Kim, Dissimilar laser welding of a CoCrFeMnNi high entropy alloy to 316 stainless steel, Scr Mater 206 (2022) 114219. https://doi.org/10.1016/J.SCRIPTAMAT.2021.114219.

[51] J.P. Oliveira, A. Shamsolhodaei, J. Shen, J.G. Lopes, R.M. Gonçalves, M. de Brito Ferraz, L. Piçarra, Z. Zeng, N. Schell, N. Zhou, H. Seop Kim, Improving the ductility in laser welded joints of CoCrFeMnNi high entropy alloy to 316 stainless steel, Mater Des 219 (2022) 110717. https://doi.org/10.1016/J.MATDES.2022.110717.

[52] J.T. Tharappel, J. Babu, Welding processes for Inconel 718- A brief review, IOP Conf Ser Mater Sci Eng 330 (2018) 012082. https://doi.org/10.1088/1757-899X/330/1/012082.

[53] T. Sonar, V. Balasubramanian, S. Malarvizhi, T. Venkateswaran, D. Sivakumar, An overview on welding of Inconel 718 alloy - Effect of welding processes on microstructural evolution and mechanical properties of joints, Mater Charact 174 (2021) 110997. https://doi.org/10.1016/J.MATCHAR.2021.110997.

[54] Donald Peckner, I. M. Bernstein, Handbook of Stainless Steels, McGraw-Hill Book Company, New York, 1977.

[55] D. Afonso, J.G. Lopes, Y.T. Choi, R.E. Kim, N. Schell, N. Zhou, H.S. Kim, J.P. Oliveira, Dissimilar laser welding of an as-rolled CoCrFeMnNi high entropy alloy to Inconel 718 superalloy, Opt Laser Technol 180 (2025) 111427. https://doi.org/10.1016/J.OPTLASTEC.2024.111427.

[56] A. Mortezaie, M. Shamanian, An assessment of microstructure, mechanical properties and corrosion resistance of dissimilar welds between Inconel 718 and 310S austenitic stainless steel, International Journal of Pressure Vessels and Piping 116 (2014) 37–46. https://doi.org/10.1016/J.IJPVP.2014.01.002.

[57] M.G. Jo, H.J. Kim, M. Kang, P.P. Madakashira, E.S. Park, J.Y. Suh, D.I. Kim, S.T. Hong, H.N. Han, Microstructure and mechanical properties of friction stir welded and laser welded high entropy alloy CrMnFeCoNi, Metals and Materials International 24 (2018) 73–83. https://doi.org/10.1007/S12540-017-7248-X/METRICS.

[58] S. Li, Q. Wei, Y. Shi, C.K. Chua, Z. Zhu, D. Zhang, Microstructure Characteristics of Inconel 625 Superalloy Manufactured by Selective Laser Melting, J Mater Sci Technol 31 (2015) 946–952. https://doi.org/10.1016/J.JMST.2014.09.020.

[59] B. Kagay, K. Findley, S. Coryell, A.B. Nissan, Effects of alloy 718 microstructure on hydrogen embrittlement susceptibility for oil and gas environments,

Https://Doi.Org/10.1080/02670836.2016.1139225 32 (2016) 697–707. https://doi.org/10.1080/02670836.2016.1139225.

[60] K. Sajun Prasad, S.K. Panda, S.K. Kar, M. Sen, S.V.S.N. Murty, S.C. Sharma, Microstructures, Forming Limit and Failure Analyses of Inconel 718 Sheets for Fabrication of Aerospace Components, J Mater Eng Perform 26 (2017) 1513–1530. https://doi.org/10.1007/S11665-017-2547-4/METRICS.

2024

Rodrigo Pedro

DISSIMILAR WELDING OF AS-CAST Al-CoCrFeNi$_{2.1}$ EUTECTIC HIGH ENTROPY ALLOY WITH 316 STAINLESS STEEL AND INCONEL 718

NOVA SCHOOL OF SCIENCE & TECHNOLOGY